Mapping thin resistors and hydrocarbons with marine EM methods, Part II — Modeling and analysis in 3D

Chester J. Weiss[1] and Steven Constable[2]

ABSTRACT

The electromagnetic fields surrounding a thin, subseabed resistive disk in response to a deep-towed, time-harmonic electric dipole antenna are investigated using a newly developed 3D Cartesian, staggered-grid modeling algorithm. We demonstrate that finite-difference and finite-volume methods for solving the governing curl-curl equation yield identical, complex-symmetric coefficient matrices for the resulting $N \times N$ linear system of equations. However, the finite-volume approach has an advantage in that it naturally admits quadrature integration methods for accurate representation of highly compact or exponentially varying source terms constituting the right side of the resulting linear system of equations. This linear system is solved using a coupled two-term recurrence, quasi-minimal residual algorithm that does not require explicit storage of the coefficient matrix, thus reducing storage costs from $22N$ to $10N$ complex, double-precision words with no decrease in computational performance. The disk model serves as a generalized representation of any number of resistive targets in the marine environment, including basaltic sills, carbonates, and stratigraphic hydrocarbon traps. We show that spatial variations in electromagnetic phase computed over the target are sensitive to the disk boundaries and depth, thus providing a useful complement to the usual amplitude-versus-offset analysis. Furthermore, we estimate through the calculation of Fréchet sensitivity kernels those regions of the 3D model which have the greatest effect on seafloor electric fields for a given source/receiver configuration. The results show that conductivity variations within the resistive disk have a stronger influence on the observed signal than do variations in the surrounding sediment conductivity at depth.

INTRODUCTION

After languishing for many years as an academic curiosity, the marine controlled-source electromagnetic method has recently and rapidly developed into a promising industrial tool for mapping resistive, subseabed geological structures, particularly hydrocarbon reservoirs (e.g., MacGregor and Sinha, 2000; Eidsmo et al., 2002; Ellingsrud et al., 2002; Johansen et al., 2005; Constable, 2006; Srnka et al., 2006). The commercialization of this method relied heavily on decades of academic development of instrumentation (Webb et al., 1985; Cox et al., 1986; Sinha et al., 1990; Constable et al., 1998) and numerical modeling techniques (Chave and Cox, 1982; Cheesman et al., 1987; Yu and Edwards, 1992; Everett and Edwards, 1993; Newman and Alumbaugh, 1995; Unsworth and Oldenburg, 1995; Flosadottir and Constable, 1996; Smith, 1996; Badea et al., 2001).

Although the magnetotelluric (MT) method can be used in the marine environment to map geological structure (e.g., Hoversten et al., 2000; Key et al., 2006), induced MT electric fields are largely horizontal and thus insensitive to thin, subhorizontal resistive structures. In contrast, electric fields generated by horizontal, electric controlled-source transmitters generate significant charge buildup on the broad horizontal faces of thin, resistive targets. Constable and Weiss (2006) investigated this effect primarily in the context of a 1D earth structure, verifying that the joint Occam inversion (Constable et al., 1987) of controlled-source and MT data can provide reasonable constraints on the depth and thickness of a thin, resistive target. Preliminary analysis of the canonical disk model (100 Ωm, 100 m thick, variable radius, 1 km deep in 1-Ωm sediments) showed that the inline 3D response of the disk matches the 1D response away from the disk edge, where the solution slowly transitions from the three-layer response on the disk to the half-space response off the

disk. Analysis of an idealized anticlinal trap by Um (2005) illustrated the complicated 3D distribution of electromagnetic fields on and around the seabed in response to time-harmonic and transient source antennas. In contrast, we continue the analysis of the simpler disk model and introduce structural complications in a parametric fashion so their individual effects may be more easily identified.

The analysis is based on a newly developed, 3D Cartesian finite-volume solution to the time-harmonic Maxwell equations in the inductive limit. It builds upon the very early work of Yee (1966) whereby a staggered Cartesian grid is introduced, on whose edges the electric fields are computed. The first applications of this approach for simulation of electromagnetic prospecting data appear in Wang and Hohmann (1993) and Newman and Alumbaugh (1995). Since then, alternative solution methodologies have focused on unstructured finite-element grids for greater model flexibility (Badea et al., 2001) and coupled vector-scalar potentials (Badea et al., 2001; Haber and Ascher, 2001) to avoid complexities arising from discretization of discontinuous field variables (e.g., normal electric field at conductivity interfaces). We revisit the original staggered-grid formulation, in terms of the electric field, and develop a finite-volume solution based upon this discretization.

We structure the paper as follows. Elements of the numerical solution are presented first, with a discussion on the governing equations, various approaches to their solution using a staggered grid, and algorithmic details on obtaining those solutions at a minimal computational cost. Examples are given that demonstrate the accuracy of the solution, the effects of various adjustable parameters (such as mesh size), and the difference in computational performance when the matrix-free algorithm is faced off against a Harwell-Boeing stored-matrix algorithm. Next, we investigate the fully 3D response of the canonical disk model (Constable and Weiss, 2006) and structural variants therein by introducing a 90° notch and a 200-m vertical offset fault at the disk's center. Last, we investigate the sampling volume of a seabed electric field measurement in the presence of the unaltered disk by analyzing isosurfaces of the Fréchet sensitivity kernel. Conclusions and summary remarks are provided at the end of the paper.

ELEMENTS OF THE NUMERICAL SOLUTION

Assuming an $e^{i\omega t}$ time dependence, uniform magnetic permeability $\mu_0 = 4\pi \times 10^{-7}$ H/m and a scalar conductivity $\sigma(x,y,z)$, the differential form of Ampere's and Faraday's laws can be combined in the low-frequency limit to form a second-order partial differential equation in terms of the electric field vector $\mathbf{E}$ and some arbitrary electric source-current density $\mathbf{J_s}$:

$$\nabla \times \nabla \times \mathbf{E} + i\omega\mu_0\sigma\mathbf{E} = -i\omega\mu_0\mathbf{J_s}. \quad (1)$$

Furthermore, given some reference model σ_0 for which solutions $\mathbf{E}^0$ to equation 1 are easily and quickly available (e.g., σ_0 is a constant or a function of depth z only), equation 1 can be recast in terms of a scattered-field formulation whereby the scattered field $\mathbf{E}' = \mathbf{E} - \mathbf{E}^0$ solves the related equation

$$\nabla \times \nabla \times \mathbf{E}' + i\omega\mu_0\sigma\mathbf{E}' = -i\omega\mu_0(\sigma - \sigma_0)\mathbf{E}^0. \quad (2)$$

The solution to equation 1 is then given by summing the scattered $\mathbf{E}'$ and primary $\mathbf{E}^0$ solutions. Although a full treatment of the relative merits of the total-field versus scattered-field formulations is beyond the scope of this paper, experience with the scattered-field formulation for compact sources, such as the electric dipole or extended

electric bipole in the marine CSEM problem, has shown that the scattered-field formulation tends to yield consistently satisfactory results. In the calculations that follow, the reference model is taken as a 3.3-S/m whole space, over which analytic formulas of the primary electric and magnetic fields are known for an electric dipole source (Ward and Hohmann, 1988):

$$\mathbf{J_s} = Id\mathbf{s}\,\delta(\mathbf{r} - \mathbf{r}_0). \quad (3)$$

Note that the source singularity in the primary electric field does not appear in the 3D problem (equation 2), because the source is located in the 3.3-S/m seawater region of the 3D model and, hence, $\sigma(\mathbf{r}) - \sigma_0 = 0$. Working with the scattered-field formulation has the advantage that magnetic dipole sources can be considered with relative ease since the analytic formulas for the primary fields are similarly easy to derive and inexpensive to compute (Ward and Hohmann, 1988). These sources are important in the calculation of adjoint-based Fréchet derivatives of magnetic-field data, in addition to the evaluation of real inductive source (Cheesman et al., 1990, 1993).

Discretization of the governing equation

The numerical solution we compute is based on the staggered-grid discretization (Figure 1) of electric and magnetic fields over a Cartesian tensor-product grid (Yee, 1966). Various authors have derived, discussed, and applied the second-order finite-difference solution based on this discretization (see Wang and Hohmann, 1993; Mackie et al., 1994; Newman and Alumbaugh, 1995); indeed, this problem is well documented in the literature. To summarize, two alternative but equivalent methods have emerged for computing the right side and matrix coefficients for the finite-difference linear system: one based on the integral form of Maxwell's equations, the other on the differential form (Figure 2).

In contrast, we introduce the concept of a control volume and compute the frequency-domain finite-volume solution to equation 2 (see Madsen and Ziolkowski, 1988, 1990, for the time-domain solution using coupled first-order equations). The basic idea behind the finite-volume approach is to introduce a set of spatially continuous control volumes. Within each control volume, the dependent variable of some differential equation is defined on a set of Gauss points. Over each, the differential equation is volume integrated. Depending on the operator of the differential equation, the volume integral is rewritten as a surface integral which then couples the nodal values within one control volume to those of its neighbors. Note that these surface integrals are on the perimeter Γ of the volume Ω, in contrast to the surface integrals in Figure 2, which are taken over the flaps of the staggered grid stencil. A linear system of equations results. While the same matrix coefficients can be derived from a finite-difference approach (either through successive line integrations or the introduction of a truncated series expansion), the concept of a control volume underlies the uniqueness of finite volumes as a numerical approach, even for staggered-grid discretizations (Yee and Chen, 1997). There have been scattered attempts in the literature (e.g., Wang and Fang, 2001; Weiss and Newman, 2002) where volume-integration formulas have been exploited in a piecemeal approach toward developing finite-difference systems of linear equations. The primary difference between these earlier attempts and the present is the consistency with which the control-volume concept is applied and the recognition of the freedom it provides in approximating the source terms of the governing equation.

For the problem at hand (equation 2) we exploit the identity

$$\int_{\Omega} \nabla \times \mathbf{A} \, d\Omega = \int_{\Gamma} \mathbf{n} \times \mathbf{A} \, d\Gamma, \qquad (4)$$

which transforms the volume integral of the curl of a vector field $\mathbf{A}$ over Ω into a surface integral over Γ where $\mathbf{n}$ is the outward-pointing unit normal. Substituting $\nabla \times \mathbf{E}$ into equation 2 results in

$$\int_{\Gamma} \mathbf{n} \times (\nabla \times \mathbf{E}') \, d\Gamma + i\omega\mu_0 \int_{\Omega} \sigma\mathbf{E}' d\Omega$$

$$= -i\omega\mu_0 \int_{\Omega} (\sigma - \sigma_0)\mathbf{E}^0 \, d\Omega \qquad (5)$$

for each of the control volumes Ω within the tensor product grid. Note that equation 5 is still a fully coupled differential equation with vector components over the three Cartesian axes. To get a set of three coupled scalar equations, we take the projection of this equation onto those axes and find, for example, the $\hat{y}$-component as

$$\hat{y} \cdot \int_{\Gamma} \mathbf{n} \times (\nabla \times \mathbf{E}')d\Gamma + i\omega\mu_0 \int_{\Omega} \sigma E'_y d\Omega$$

$$= -i\omega\mu_0 \int_{\Omega} (\sigma - \sigma_0)E^0_y d\Omega. \qquad (6)$$

Inspection of equations 5 and 6 reveals that only the first integral contains the coupling terms, as expected. Also, inspection of the surface integral in equation 6 hints at a strategy for definition of the control volume.

We now lay down some definitions. Define the Yee grid by a set of N_x nodes in x, N_y nodes in y, and N_z nodes in z. Components of $\mathbf{E}$ lie at the midpoints of edges within the Cartesian mesh defined by these nodes (see Figure 1). This results in, for example, $N_x \times (N_y - 1) \times N_z$ edges where the $\hat{y}$-component of electric field is defined. Let the control volumes for the $\hat{y}$ equations (Figure 3) be the region defined by

$$\frac{1}{2}(x_{i-1} + x_i) < x < \frac{1}{2}(x_i + x_{i+1})$$

$$y_j < y < y_{j+1}$$

$$\frac{1}{2}(z_{k-1} + z_k) < z < \frac{1}{2}(z_k + z_{k+1}) \qquad (7)$$

for $i = 2, \ldots, N_x - 1$, $j = 1, \ldots, N_y - 1$ and $k = 2, \ldots, N_z - 1$. This definition of the control volumes places one $\hat{y}$-component of the electric field at the center of the volume Ω and provides access to first-order estimates of the various partial derivatives of $\mathbf{E}'$ appearing in equation 6 on the boundary Γ. Using a local enumeration (Figure 1) for compactness, the left side of equation 6 is given as

$$\tilde{\Delta}z_k(u_1 - u_2 - u_3 + u_4) + \tilde{\Delta}x_i(w_1 - w_2 - w_3 + w_4)$$

$$+ i\omega\mu_0 S_\Omega v_3 + \tilde{\Delta}x_i\Delta y_j \left(\frac{v_3 - v_1}{\Delta z_{k-1}} - \frac{v_5 - v_3}{\Delta z_k} \right)$$

$$+ \Delta y_j\tilde{\Delta}z_k \left(\frac{v_3 - v_2}{\Delta x_{i-1}} - \frac{v_4 - v_3}{\Delta x_i} \right), \qquad (8)$$

where S_Ω is the volume conductance $\int \sigma d\Omega$ and

$$\tilde{\Delta}x_i = \frac{1}{2}(\Delta x_{i-1} + \Delta x_i)$$

$$\tilde{\Delta}y_j = \frac{1}{2}(\Delta y_{j-1} + \Delta y_j) \quad \tilde{\Delta}z_k = \frac{1}{2}(\Delta z_{k-1} + \Delta z_k).$$

This expression yields 13 matrix coefficients identical to the scaled, or symmetrized, coefficients appearing in a finite-difference solution to equation 2 (Newman and Alumbaugh, 1995). For the $\hat{x}$ and $\hat{z}$ projections of equation 5, two additional sets of analogous control volumes are constructed, each centered on the $\hat{x}$ and $\hat{z}$ edges of the Yee grid, respectively. An $N \times N$ complex symmetric matrix with 13 nonzero entries per row results, where the number of degrees of freedom (or unknowns) in the linear system is $3N_xN_yN_z - N_xN_y - N_xN_z - N_yN_z$ less the components of $\mathbf{E}'$ on the edges of the mesh, to which a homogeneous Dirichlet condition is applied.

Thus, it would appear at first glance that little has been gained by recasting the problem in terms of the finite-volume framework; the same matrix results. Evaluation of the volume integral on the left side gives some justification to arithmetic averaging of the conductivity σ around some edge, assuming a locally linear behavior to the electric field. There may be some theoretical benefit, yet to be determined, in illustrating the equivalence, as we have done, of these low-order finite-difference and finite-volume matrices (Mattiussi, 1997). However, our aim is not to dwell on the equivalence of the matrices but rather to point out that the finite-volume discretization offers one additional bit of freedom in constructing the linear system: integration of the source term in building the right side of the linear system.

In equation 6 and its counterparts for the $\hat{x}$- and $\hat{z}$-components, the source term is also integrated over a control volume. A finite-difference formulation admits no such operation; the primary field $\mathbf{E}^0$ components are simply evaluated on the edges of the staggered grid. For primary fields with large curvature, such as near a dipole transmitter, the freedom to integrate primary fields to higher accuracy offers the possible mechanism to minimize grid artifacts and error in the numerical solution. In the next section, we investigate the effectiveness of source integration to minimize grid artifacts.

Solution verification

For the numerical exercises that follow, an n-point Gaussian quadrature is used to evaluate the source integrals (Figure 4). The linear system is solved using the iterative quasi-minimal residual (QMR) method of Freund and Nachtigal (1994) stabilized by a two-term coupled recurrence and preconditioned using simple Jacobi scaling. As a first example, numerical solutions for a horizontal electric dipole 100 m over a 1-Ωm half-space are compared to analytic solutions. One-point Gaussian quadrature ($n = 1$ in Figure 4) was used on the source terms. The mesh consisted of a uniform $81 \times 81 \times 81$ node grid over $|x|,|y|,|z| < 2$ km with the seafloor taken at $z = 0$. Quasi-analytic solutions were computed based on Hankel transforms (Chave, 1983) of the magnetic vector potential (see Baños, 1966, for a closely related approach using electric hertz potentials). The presence of an $\hat{x}$-directed dipole over the seabed gives rise to six components of the electromagnetic field along the inline $\hat{x}$ and broadside $\hat{y}$-directions (Figure 5). For code validation purposes, both the in-phase and quadrature components of the solutions are presented (Figure 6), although in practice the complex amplitude of the fields is the quantity typically used for subsurface interpretation (e.g., Eidsmo et al., 2002). Recall that the electric-field components are sampled along conductivity boundaries of the mesh (Figure 1)

and, as such, the horizontal electric fields in Figure 6 lie directly on a grid boundary coincident with the seafloor. Vertical electric fields, however, are not directly available at the seafloor; they are sampled one-half a grid spacing above and below. Thus, for comparison pur-
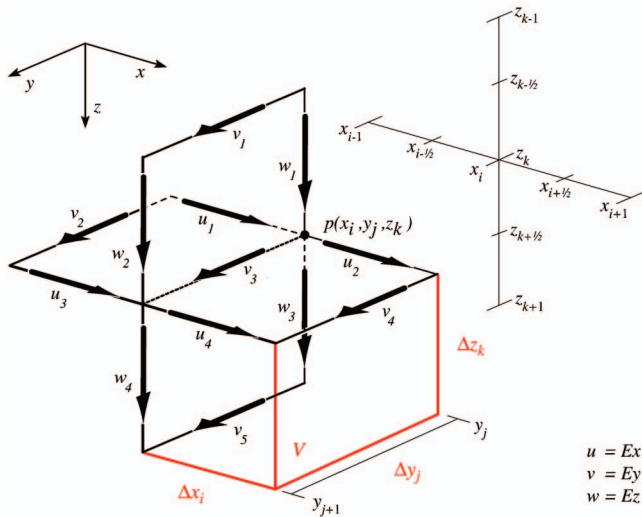

Figure 1. The basic staggered-grid paddle wheel stencil representing the components of the vector field $\mathbf{E} = \hat{x}u + \hat{y}v + \hat{z}w$ and their locations within the Cartesian tensor-product grid. Shown is the stencil used for y-components of the governing equation. Analogous stencils are constructed for the remaining x- and z-components. Material properties (e.g., conductivity) are assigned to grid cells V and assumed constant throughout the cell volume.
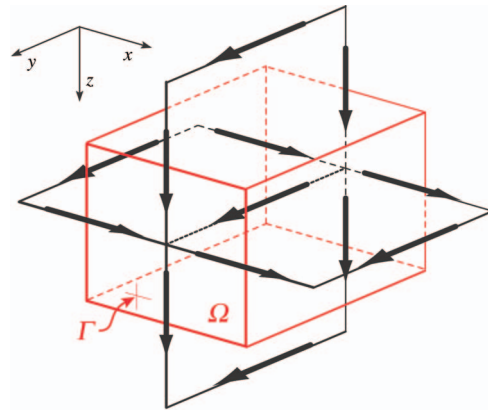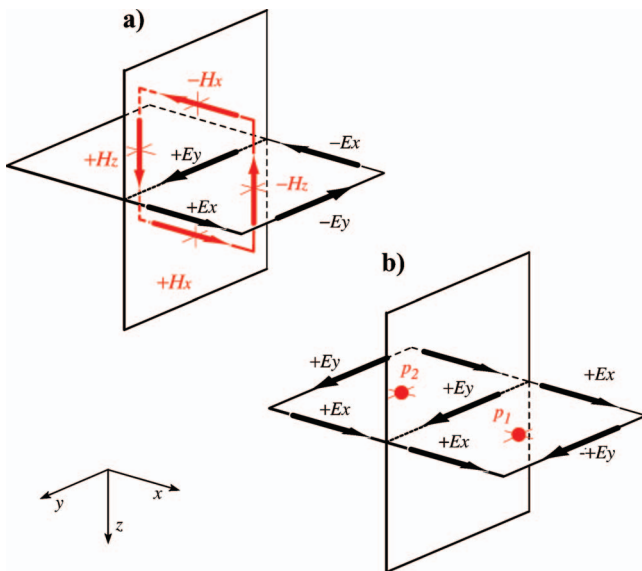

Figure 2. Two approaches to discretization of the $\nabla \times \nabla \times$ operator via finite differences. (a) Successive line integration, first on $\mathbf{E}$ to arrive at normal $\mathbf{H}$ on the flaps of the paddle, then on $\mathbf{H}$ to arrive at normal $\mathbf{E}$ at the center (and thus eliminating an explicit $\mathbf{H}$-dependence). (b) Successive differentiation of $\mathbf{E}$ components, first to the centers of the paddle flaps (e.g., points p_1 and p_2), then again to the paddle center.

poses, the numerical and quasi-analytic solution for the vertical electric field is sampled immediately off the seabed at the midpoint of vertical grid edges.

A given magnetic-field component at the center of a cell face can be derived from application of Faraday's law because the electric fields at the face edges are available as products of the finite-volume/difference solution. Components of the magnetic field elsewhere in the mesh are computed by trilinear interpolation over eight such applications at points forming a small Cartesian volume, which, it turns out, is identical with the control volume used for finite-volume integration (Figure 4). We see that the poorest agreement between the

Figure 3. Control volume Ω with bounding surface Γ for finite-volume discretization of the y-component of the governing equation. Analogous control volumes are constructed for the remaining x- and z-components.
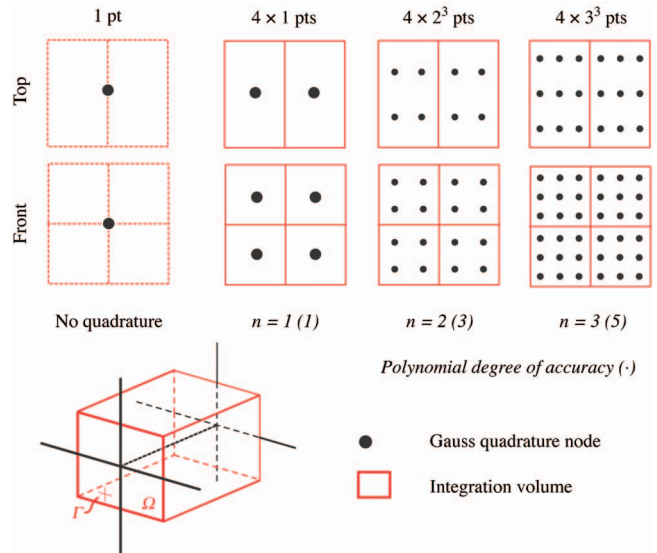

Figure 4. Location of points where the source term in the governing equations is sampled for construction of the right side of the finite-difference (top, extreme left) and finite-volume (top, remaining 3) linear systems. Note that the sample point in the finite-difference formulation strictly coincides with the point at the center paddle wheel stencil.

numerical and analytic solution in Figure 6 occurs with the $\hat{y}$-component of magnetic fields — a calculation which utilizes vertical electric field components that are changing wildly in both their value and slope near the seafloor for a deep-towed transmitter.

The second set of numerical experiments (Figure 7) involves placing the dipole transmitter directly on the seafloor to simulate the response of an actual trawled transmitter source (Cox et al., 1986) or to provide an adjoint solution for calculation of Fréchet sensitivity kernels. In this case we investigate the effect of mesh size ($N \times N \times N$) and integration order on the accuracy of the numerical solution when the dipole source is located at some arbitrary position within the mesh. Mesh spacing is kept uniform, as before, over a 4-km cube. However, coordinates of mesh nodes have been translated 20 m in x and y, placing the transmitter coordinates $x, y, z = 0$ somewhere in the interior of a cell face on the seabed. Note that when $N = 101$, the transmitter lies directly in the center of 40×40-m cell face.

Inspection of the radial component E_ρ of the electric field on the seabed (see Figure 5) reveals that when quadrature is ignored ($n = 0$), as is done with finite differences, the effect is to strongly bias the numerical solution because of the asymmetric sampling of the primary field solution $\mathbf{E}^0$ at the grid edges (Figure 7a). When the source is placed on a symmetry plane in the center of a cell face, ($n = 0$, $N = 101$) the results are generally in good agreement with the analytic solution. In contrast, the finite-volume approach of integrating the primary field with low-order Gaussian quadratures ($n = 1,2$) consistently improves the coarse mesh solutions. Note that higher-order integration ($n = 3$) simply reintroduces a new form of grid bias, thus suggesting a compatibility requirement between the truncation order of the source terms and field variables in equation 6. Similar behavior is observed with the azimuthal component of the electric field (Figure 7b).

As mentioned earlier, the $N \times N$ linear system of equations arising from finite-volume discretization of equation 2 is solved using a coupled two-term recurrence formulation of the QMR method of Freund and Nachtigal (1994). The coupled two-term recurrence refers to the algorithm by which the basis vectors of the Krylov subspace are formed. Preference for coupled two-term recurrence algorithms over the mathematically equivalent three-term algorithm is based on a wealth of evidence for improved numerical stability over a broad range of Krylov subspace solvers, including QMR (Freund and Nachtigal, 1991), conjugate gradients (Woźniakowski, 1980), and biconjugate gradients (Langtangen and Tveito, 1988). More importantly, though, we note that the QMR algorithm bears an important similarity to other Krylov-subspace iterative solvers. Only the action of the coefficient matrix on some vector is required at each QMR iterate; explicit matrix storage is not required. As such, we compute the simple products and differences that constitute matrix elements (see equation 8) at each QMR iterate, with the exception of the matrix diagonal, which is computed once at the outset of the QMR algorithm and then reused within as a Jacobi preconditioner. Extending the early work of Weiss (2001), we find the performance trade-off is nearly even between recalculation of matrix elements and memory management (cache hits) of the large arrays arising from sparse matrix storage

and not dependent on a specific computer architecture (Figure 8). Memory requirements for the two approaches are dramatically different. As implemented here, the matrix-free approach requires storage of $10N$ complex double-precision words. The Harwell-Boeing sparse matrix storage (Duff et al., 1989) used for the timing results in Figure 8 adds an additional $12N$ complex double-precision words, bringing the total to $22N$. In terms of mesh size, the stored-matrix formulation can accommodate a $120 \times 120 \times 120$ node mesh on a 32-bit operating system, whereas the matrix-free formulation can accommodate a $200 \times 200 \times 100$ node mesh in the same 2 GB of main memory.
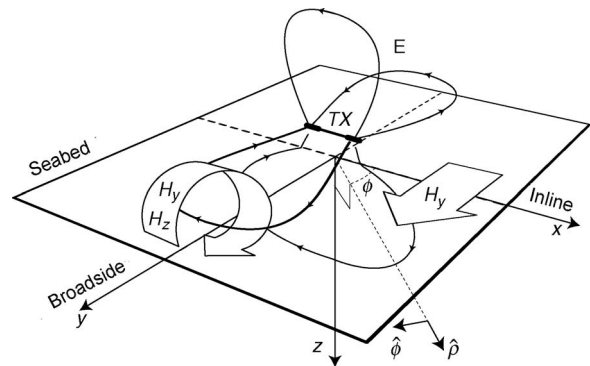

Figure 5. Geometry and experimental nomenclature for the fields surrounding an x-directed horizontal electric dipole (TX) above the seabed. Note that for the inline geometry, only the x- and z-components of electric field are present; the broadside geometry results in a purely x-directed electric field. Thus, a nonzero y component arises from either intermediate azimuths ϕ or the presence of 3D electrical structure.
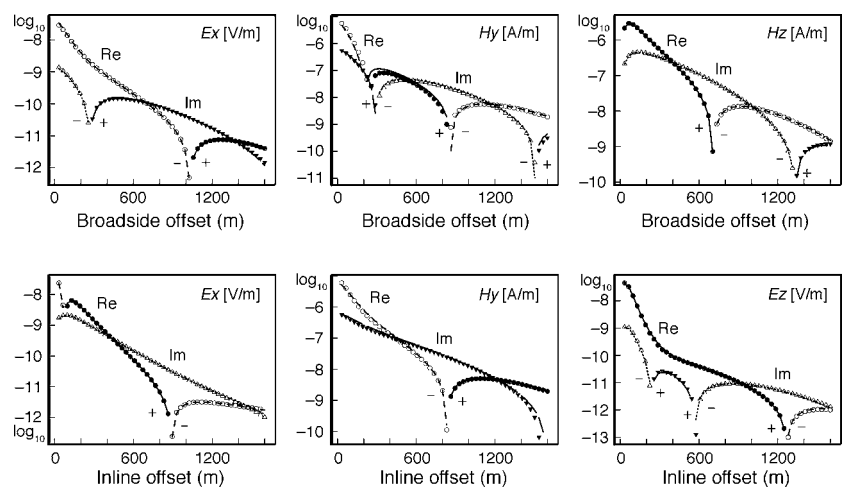

Figure 6. Analytic (lines) and finite-difference (symbols) solutions for the horizontal broadside and inline electromagnetic fields on the seabed $z = 0$ because of an $\hat{x}$-directed, 1-Hz electric dipole source positioned 100 m above the seafloor. Seawater conductivity is taken as 3.3 S/m, sediment as 1.0 S/m. Discontinuity of vertical electric field E_z at the seabed requires sampling at $z \neq 0$; shown in the lower right is E_z at $z = -25$ m, the midpoint of the first row of grid cells above the seafloor.

Remarks on the current implementation

We have shown that the finite-difference/finite-volume approach to modeling seafloor structure produces accurate solutions with a
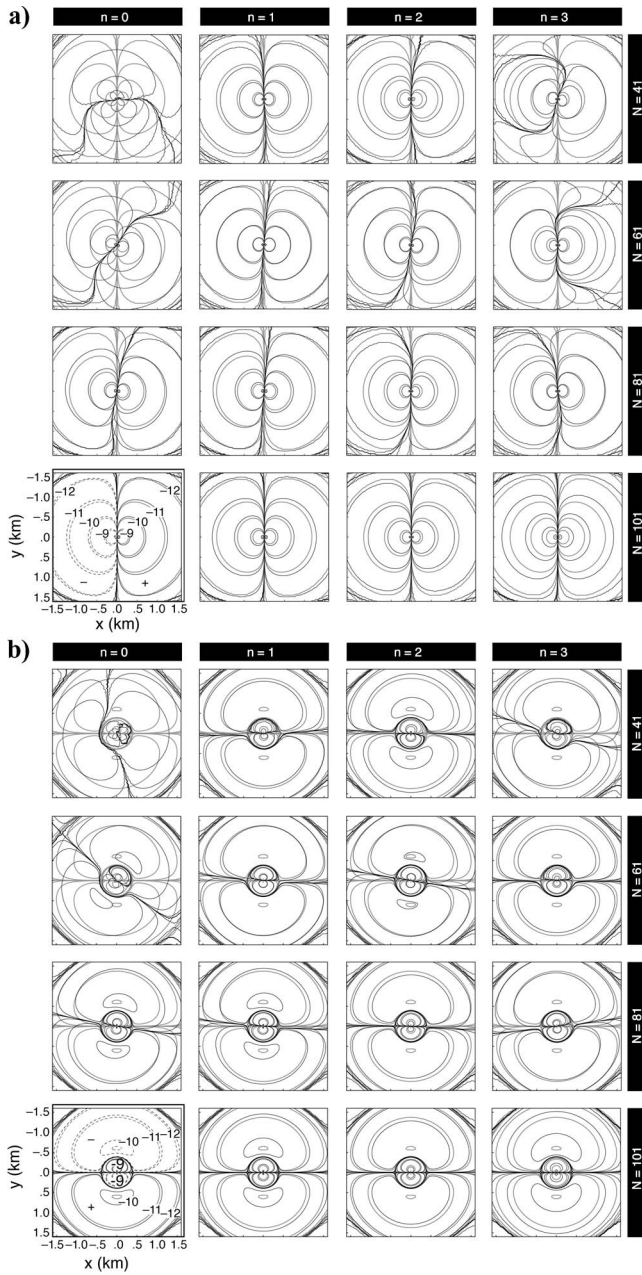

Figure 7. (a) Isolines of E_ρ on the seabed $z = 0$ for an $\hat{x}$-directed electric dipole source at the origin $x = y = z = 0$ as a function of grid size, $N \times N \times N$, (rows) and quadrature order, n, (columns). Annotations in $\log_{10}$V/m for numerical (black) and analytic (gray) solutions appear in the lower left ($n = 0$, $N = 101$) along with dashed and solid lines representing regions of negative and positive E_ρ, respectively. (b) Isolines of E_ϕ on the seabed $z = 0$ for an $\hat{x}$-directed electric dipole source at the origin $x = y = z = 0$ as a function of grid size, $N \times N \times N$, (rows) and quadrature order, n, (columns). Annotations in $\log_{10}$V/m for numerical (black) and analytic (gray) solutions appear in the lower left ($n = 0$, $N = 101$) along with dashed and solid lines representing regions of negative and positive E_ϕ, respectively.

reasonable expenditure of computational and memory resources, but there are limitations to this approach. For example, although it would be possible to include an air layer in the computation, we have chosen not to do so because the large conductivity contrast between seawater and air reduces the condition number of the problem significantly. We do not view this as a huge restriction; as we have shown, a good deal of insight into the way electromagnetic fields interact with target structures can be obtained without considering the effect of the air. To a good approximation, the effect of the air layer serves to limit the source-receiver ranges over which seafloor electric fields are dominated by subseafloor structure, and for flat seafloor this may easily be predicted by simple closed-form solutions (e.g., Constable and Weiss, 2006; Bannister, 1984). Nonflat seafloor (i.e., bathymetry) can be modeled using finite-difference methods, but again this puts large demands on the size of the mesh. Finite-element methods are probably a better choice if bathymetric effects are of primary concern. One consideration in this respect is that finite-difference methods work well for fairly uniform meshes made up of nearly equal element volumes.

INVESTIGATION OF THE CANONICAL DISK MODEL

Using the finite-volume approach described above, we investigate further the 3D response of the canonical model of Constable and Weiss (2006). This model is representative of a large, deepwater oil or gas field, not unlike the ones studied by Ellingsrud et al. (2002) and Johansen et al. (2005). It consists of a reservoir represented by a 100-m-thick horizontal disk of radius 2-km and resistivity 100 Ωm. The reservoir body is buried at a depth of 1 km within a half-space of 1 Ωm water-saturated sediment. The higher resistivity of the target disk is representative of the replacement of porewater by resistive hydrocarbons, but the reader is cautioned that high resistivities could also result from, for example, basaltic sills, carbonates, or evaporite layers. Current applications of the controlled-source EM methods
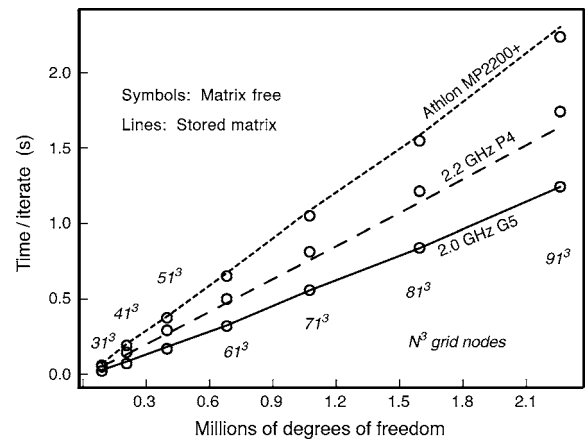

Figure 8. Platform-independent linear scaling of CPU time per QMR iterate as a function of degrees of freedom in the linear system. Average rates for 100 QMR iterations of the matrix-free (symbols) and the stored-matrix formulations (lines) are shown.

are designed to distinguish whether the weak seismic response associated with the presence of oil or gas in potential reservoirs is associated with resistive (thus prospective) or conductive (less prospective) structures. We note, however, that while basalts, etc., present confounding interpretations in the context of reservoir characterization, they also present challenges to seismic characterization because of their high seismic impedance contrast with the surrounding sediments. This effectively masks subtle stratigraphic structures lying within or beneath. The ability to image the thickness of such structures can also present an aid to exploration.

For all of the numerical results that follow, a finite-volume mesh of $161 \times 161 \times 61$ nodes was used to represent a physical volume of $|x|, |y| < 5.5$ km and $-1.5 < z < 3.0$ km with nodes evenly distributed in the x- and y-directions and the sea ($z < 0$) and subseabed ($z > 0$) regions, respectively. With this mesh spacing, the disk is approximately 58 grid cells in diameter and 1 grid cell in thickness. In spite of the crude discretization of the disk itself, we note that the short-offset response (over the disk) of the model agrees remarkably well with analytic solutions for the three-layer earth model (Constable and Weiss, 2006). Gaussian integration of the primary fields was based on the $n = 1$ point rule (see Figures 3 and 7). Target error reduction of the QMR iterative solver was kept fixed at 2×10^{-5}, bringing the final normalized residual of the linear system to approximately 4×10^{-12} in around 600 iterations. A 1-Hz transmitter is positioned 1-km off the edge of the disk, 100 m above the seafloor.

Time-harmonic field behavior

Analyzing the inline horizontal and vertical components of the electric field over the disk, Constable and Weiss (2006) illustrated a correlation between inflections in the frequency-domain fields and the edges of the disk, thus providing a potentially useful diagnostic for spatial characterization of thin resistors. Building on this, we further analyze the electric fields lying outside of the inline configuration and distributed over a 6×6-km patch of seabed centered on the disk in both the (harmonic) time-domain and frequency-domain representations. For the time-domain analysis, recall that equation 1 is based on an $e^{i\omega t}$ time dependence. As such, we consider for analysis the real part of the product of this term and the frequency-domain electromagnetic field

$$\mathrm{Re}\{\mathbf{E}(\omega)e^{i\omega t}\}$$

at a single fixed frequency $\omega = 2\pi \times 1$ Hz.

As a function of time, the electric fields on the seabed (Figure 9) exhibit behavior reminiscent of wave propagation; there is an oscillatory component and the apparent migration of cophasal fronts. However, it is important to remember that although such organization exists, it is the result of a forced oscillator (the transmitter), stimulating diffusive transport processes within the medium. The cophasal fronts, the boundary between normal and reversed polarity of the electric field, are observed to vary in their migration speed, from relatively slow in areas off the disk to relatively fast in areas directly over the disk. Thus, in a time-domain sense, observation of cophasal fronts seems to be correlated with subseabed structure. In addition to this, we note that isosurfaces of electric-field strength within the disk also oscillate with time, giving rise to a dynamic pattern over the period of oscillation of charge density on the disk's surface.

The canonical disk model

From Figure 9, we find that the cophasal front is nearly coincident with a local minimum in electric-field strength. Furthermore, the sharp local minimum in which the front resides is most clearly observed over the $+x$ side of the disk, on the side away from the transmitter. This can be explained by examining more closely the phase of the x- and y-components of the complex electric field (panel i in Figure 10a and b, respectively). Indeed, we find over this far side of the disk the $0°-315°$ isolines of phase (shaded) in the E_x component are colocated with the $0°(315°)-180°(0°)$ phase isolines in E_y. Take, for example, some phase angle $\theta(\mathbf{r})$ in this interval at one of these colocated points $\mathbf{r}$. The amplitude of the horizontal component

$$\mathrm{Re}\{\hat{x}|E_x| + \hat{y}|E_y|\}e^{i(\omega t + \theta)}$$

is then zero when $\omega t + \theta = (m \pm 1/2)\pi$ for integer m. Note that since the vertical electric field is comparatively small over the disk (see the orientation of the electric field vectors in Figure 9), the final result is a local minimum in total electric field strength, colocated with an electric-field polarity change, that appears to propagate across the $+x$ side of the disk during transmitter-phase intervals of $45°-135°$ and $225°-315°$. Furthermore, we see that within this phase interval, the relatively broad spacing between $90°$ and $45°$ isolines would result in a high apparent phase velocity over the disk, whereas their tight spacing off the disk result in lower phase velocity, as observed.

Variations on the canonical disk model

In addition to the canonical disk model, two other variants were also evaluated: a notched disk with a $90°$ sector removed and the disk sliced by a diametric normal fault with 200 m of vertical throw. As with the unaltered disk, these more complicated models also exhibit regions where the phase isolines in E_x and E_y are spatially colocated over the far side of the disk (panels ii–iv in Figure 10a and b), which, in the presence of weak vertical electric fields, result in cophasal surfaces coincident with local minima in the total electric-field amplitude (not shown). More importantly, we observe variations in the phase isolines that can be correlated with the morphology of the disk. Over the notch, isolines are more tightly spaced than elsewhere on the disk, reflecting the absence of resistive disk material. With the faulted disk, we considered the case where the far side was downthrown 200 m (panel iii) and the case where the near side was downthrown 200 m (panel iv). In both cases, the $270°-315°$ phase isolines (off the disk) were nearly identical, indicating that observations in this time interval are insensitive to whether the downthrown block was proximal or distal to the transmitter. Put another way, the result suggests an equivalence principle, which we call the *D*-equivalence, where D is defined as the integrated depth to the resistor along a path from the transmitter to the receiver — a relatively easy integral to evaluate by inspection for the models in Figure 10a and b.

For example, note that for all receivers in the region $x < 0$, such an integral remains unchanged in models i, ii, and iii, and we observe that the phase isolines in this region are also equivalent. In particu-

lar, note the location of the 90° and 270° isolines in E_x and E_y, respectively. Off the disk in the $x > 0$ region, models iii and iv share equivalent D values as well as colocated isolines for phase angles less than 315°, at least to first order. Over the disk, the differences in D for these two models are correlated with differences in phase.

Sensitivity analysis

We investigate the question of sensitivity of synthetic CSEM data over the canonical disk model to perturbations in the electrical conductivity in and around the disk, including the seawater. To do so, we exploit the adjoint method for computing Fréchet kernels in the frequency domain (McGillivray et al., 1994) and restrict our analysis to the in-phase component for simplicity. To summarize the approach, only two electric field calculations are required to evaluate the sensi-

-tivity density function throughout the model domain: one calculation based on the actual transmitter source and another calculation based on an infinitesimal virtual dipole source located at the receiver and oriented in the direction of the field component under consideration. So, if sensitivities of E_x with respect to conductivity perturbations are desired, the response of an $\hat{x}$-directed virtual dipole source on the seabed needs to be computed (see, for example, Figure 7. With these two vector solutions in hand, their inner product gives the Fréchet kernel throughout the model domain. Electric-field perturbations from conductivity perturbations over some volume are given, to first order, by the volume integral of the Fréchet kernel multiplied by the conductivity perturbation. In our analysis, we consider only the kernel and its isosurfaces in three dimensions as representations of the volume of investigation, captured by components of the
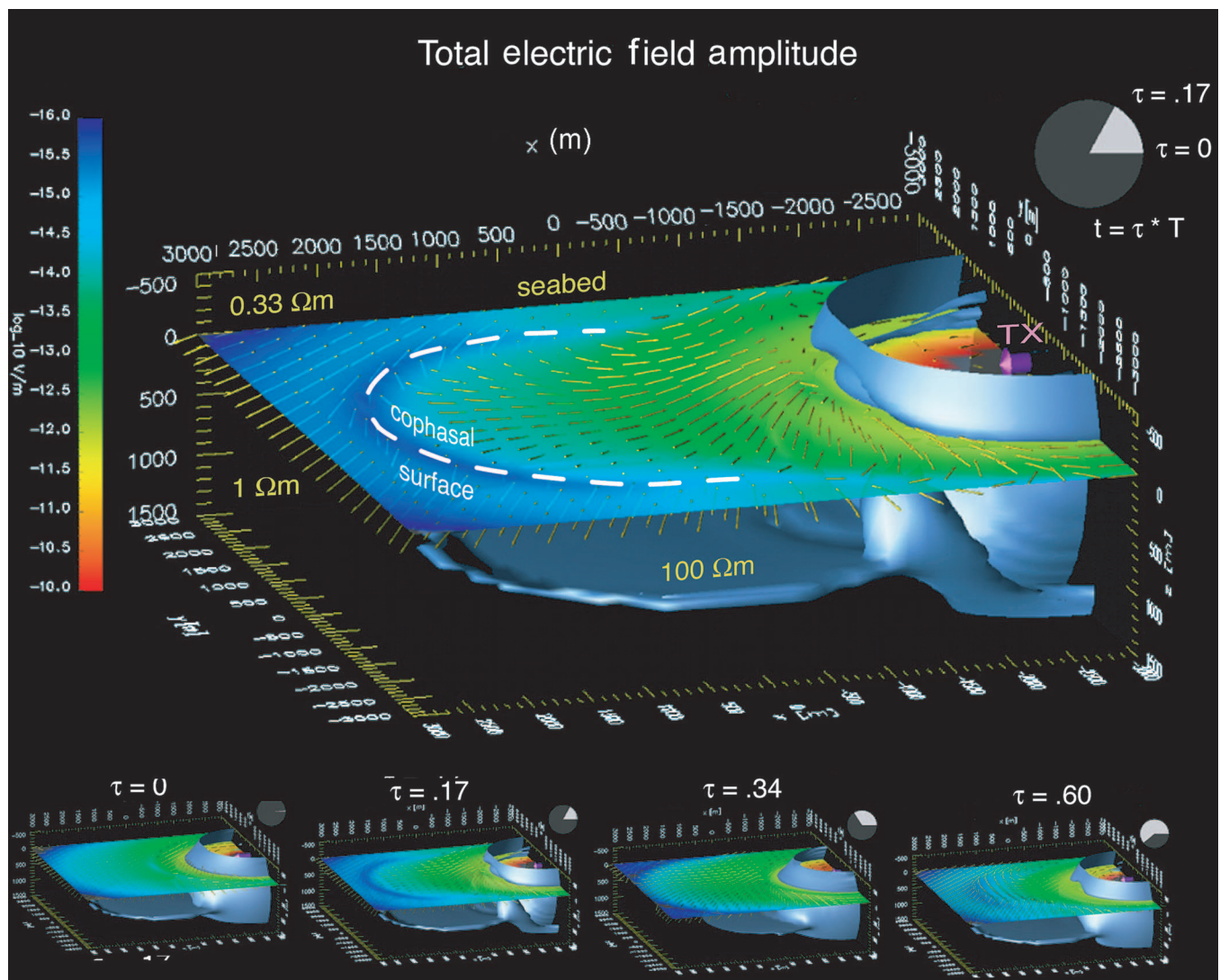

Figure 9. Time slices of electric fields in and around a 100 m thick, 2 km radius resistive disk lying 1 km beneath the sea floor. Plotted are four quantities: the 10^{-12} V/m isosurface (blue-gray), total electric field amplitude on the seabed (color scale), and electric field orientation normalized to unity (arrows). Field values are shown at four time slices τ during the $T = 1$ s period transmitter (TX) oscillation (see inset pie chart). Note the high electric field values within the disk and the corresponding elongation of the cophasal front.

electric field at a seabed receiver unit located 1 km off-center from the canonical disk. The disk itself, in this case, is excited by both in-line and broadside transmitters 1 km off the disk edge and 100 m above the seafloor.

Keeping the value of the isosurface constant (Figure 11), we obtain a qualitative assessment of the relative size of the volume of investigation for each of the six possible combinations of electric-field component and transmitter orientation. As expected by symmetry, the cross-coupled transmitter moment and electric-field (Figure 11b: $\hat{x}$-E_y; Figure 11e: $\hat{y}$-E_x) are insensitive to all geologic and seawater conductivity perturbations in the x-z plane at $y = 0$. Vertical electric-field measurements are particularly insensitive to nearly all but the disk itself in a broadside experiment (Figure 11f). However, we notethat the broadside E_x (Figure 11d) is strongly influenced by structures directly beneath the transmitter, even penetrating beneath the disk, which acts as a barrier in the other configurations. In terms of the largest control volume, the inline E_x configuration appears to dominate, but it bears mentioning that the inline E_z configuration appears to have some look-ahead capability, as evidenced by the contiguous structure emanating from the receiver location to the edge of the disk below. In all cases, the sensitivity kernel protrudes several hundred meters into the water column, suggesting that in shallow or hydrodynamically complex waters having significant haloclines or perhaps anomalous vertical mixing (e.g., in the high-latitude oceans: Aagaard and Carmack, 1989; Dickson et al., 1988), variations in seawater conductivity may be observable in seabed electric-field measurements.

DISCUSSION

The numerical solution presented here differs from previously developed ones in two significant ways: one algorithmic (the matrix-free formulation), the other formulaic (finite-volume-based integration of the right side for improved error reduction). We have demonstrated that the finite-volume approach yields the same coefficient matrix in the system of linear equations as that resulting from the finite-difference approach. This equivalency is interesting because the two approaches are fundamentally very different. However, we note that the quest for demonstrating mathematical equivalency of low-order methods for partial differential equations is a subject of current interest in the applied mathematics community (Mattiussi, 1997).

Previous authors (Edwards, 2005; Um, 2005; Constable and Weiss, 2006) have commented upon the airwave: its origins, behavior, and effect on a target's geophysical signature in one dimension. Calculation of the electromagnetic fields in the air region with the finite-volume technique presented here is accomplished by setting the region's conductivity to some nominal but nonzero value ($\sim 10^{-6}$ S/m), similar to that done with fi-

nite differences (Newman and Alumbaugh, 1995), to minimize inductive effects but preserve convergence of the linear system of equations. In our 3D calculations, we have neglected the electromagnetic coupling between the air and the conductive earth in an effort to better illuminate the inherent complexities of the electromagnetic response of thin resistive marine targets. We point out that exploration for such targets in shallow water, for example, is affected by many complications in addition to the airwave — wave motion, salinity variations, benthic currents — and it seems to us premature to consider some coupled response of the target and its environment when the 3D response of the target itself is rich in physics yet only beginning to be understood.
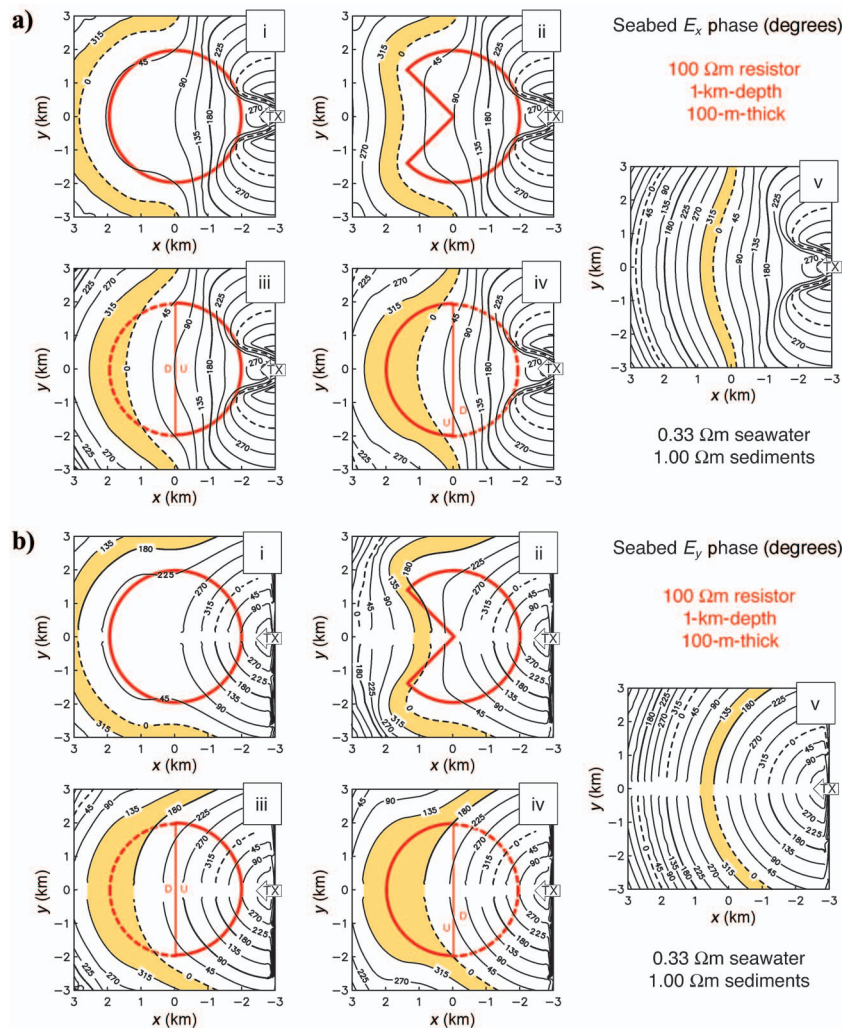

Figure 10. (a) Seabed distribution of complex phase for an E_x arising from an x-directed 1 Hz transmitter (TX) located 100 m above the seafloor at $(x, y) = (-3000, 0)$ m. Four different resistive targets are considered: (i) a 2-km-radius resistive disk 1 km below the seafloor; (ii) same disk as in (i), but with a 90° sector removed; (iii) same disk as in (i), but dissected with a normal fault with 200 m of downward throw on the $+x$ side; (iv) same as (iii) but with the downthrown side on the $-x$ half of the disk; and, (v) no disk present. (b) Seabed distribution of complex phase for E_y [see (a) for model descriptions]. Note the 180° discontinuity in phase at the $y = 0$ plane: E_y is an odd function with respect to y and, hence, the sign change in both its real and imaginary components across this plane results in a reflection about the complex origin, placing the phase in the opposite quadrant.
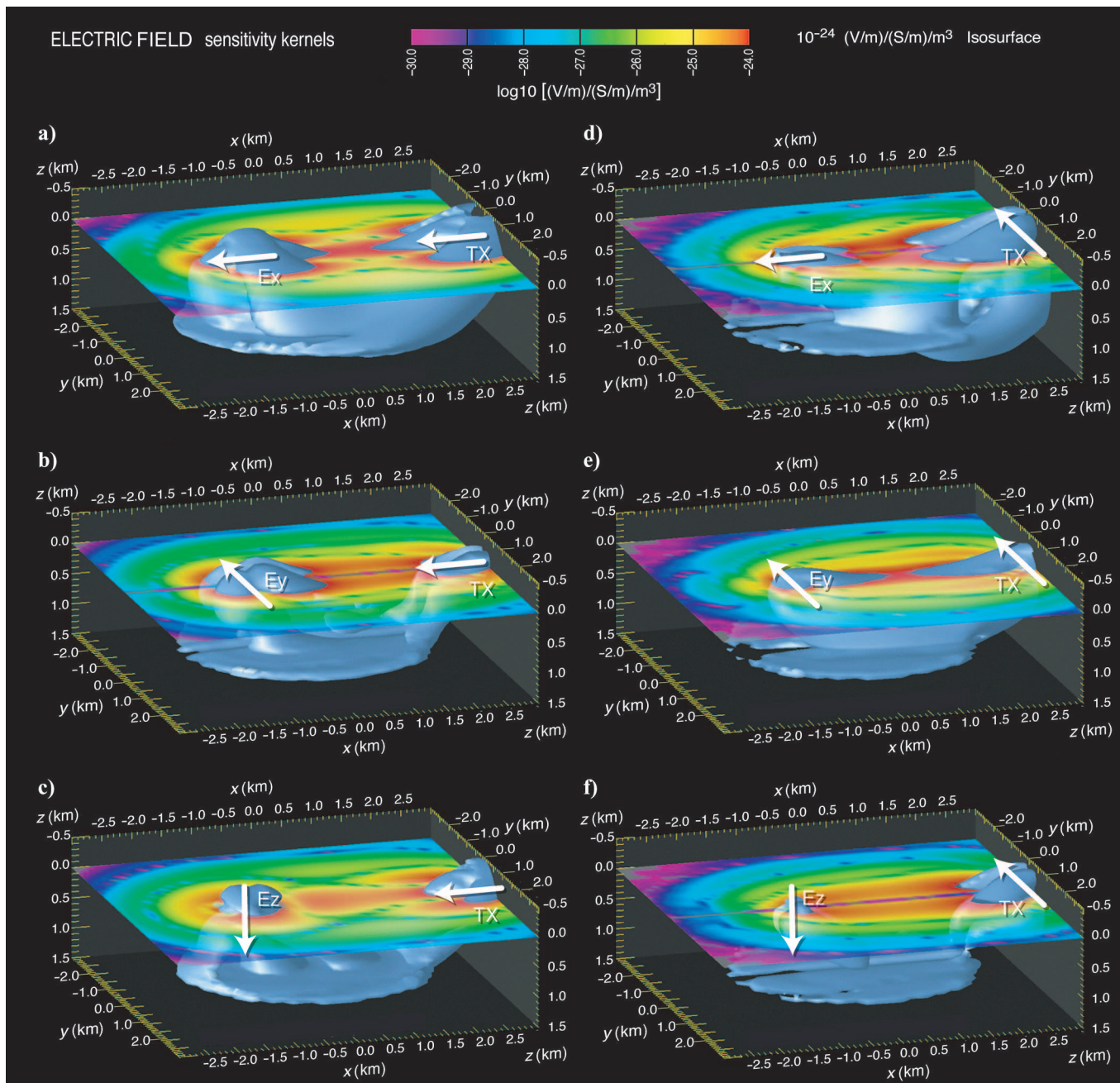
Figure 11. Sensitivity kernels for seabed in-phase electric field components measured 1 km off-center over the canonical disk model for two transmitter orientations: x-directed, pointing diskward (a-c); and y-directed, tangent to the disk (d-f). As before, the 1 Hz transmitter is located 1 km off the disk edge, 100 m above the seafloor. The seafloor receiver is offset 1 km in the negative x-direction from the disk center.

CONCLUSIONS

The numerical results demonstrate the superiority of the finite-volume discretization to the previously published finite-difference algorithms in terms of numerical accuracy and consumption of computational resources. Furthermore, we have used them to broaden the traditional interpretation approach, plotting the complex amplitude, by investigating the information content of the complex phase over the canonical disk model and some simple geometric variants. This has revealed the presence of high-velocity cophasal fronts that are localized over the disk. It has also revealed a potentially useful

equivalence principle, the D-equivalence, of the laterally integrated depth to the resistive disk.

Our sensitivity analysis for the disk model revealed several interesting facts. First, as is well known within the induction logging and crosswell logging community, the observed signal is dominated by geological heterogeneities nearest the receiver and transmitter (by reciprocity). This region of high sensitivity extends into both the water column and the subsurface, ultimately connecting up with the resistive disk, which itself is a major source of electromagnetic signal. The pattern in which these two regions connect is dependent upon

transmitter/receiver configuration. Model results confirm the strong disk response of the inline (E_x, E_z) configuration but also suggest that purely inductive broadside E_x is more sensitive to geologic structure beneath the disk that is obscured by the galvanic effects of the inline mode.

ACKNOWLEDGMENTS

REFERENCES

Aagaard, K., and E. C. Carmack, 1989, The role of sea ice and other fresh water in the Arctic circulation: Journal of Geophysical Research, **94**, 14485–14498.

Badea, E. A., M. E. Everett, G. A. Newman, and O. Biro, 2001, Finite-element analysis of controlled-source electromagnetic induction using Coulomb-gauged potentials: Geophysics, **66**, 786–799.

Bannister, P. R., 1984. New simplified formulas for ELF subsurface-to-subsurface propagation: IEEE Journal of Oceanic Engineering, **OE-9**, 154–163.

Baños, A., 1966, Dipole radiation in the presence of a conducting halfspace: Pergamon Press.

Chave, A. D., 1983, Numerical integration of related Hankel transforms by quadrature and continued fraction expansion: Geophysics, **48**, 1671–1686.

Chave, A. D., and C. S. Cox, 1982, Controlled electromagentic sources for measuring electrical conductivity beneath the oceans, 1: Forward problem and model study: Journal of Geophysical Research, **87**, 5327–5338.

Cheesman, S. J., R. N. Edwards, and A. D. Chave, 1987, On the theory of sea-floor conductivity mapping using transient electromagnetic systems: Geophysics, **52**, 204–217.

Cheesman, S. J., R. N. Edwards, and L. K. Law, 1990, A test of a short-base-line sea-floor transient electromagnetic system: Geophysical Journal International, **103**, 431–437.

Cheesman, S. J., L. K. Law, and B. St. Louis, 1993, A porosity mapping survey in Hecate Strait using a seafloor electro-magnetic profiling system: Marine Geology, **110**, 245–256.

Constable, S., 2006, Marine electromagnetic methods — A new tool for offshore exploration: The Leading Edge, **25**, 438–444.

Constable, S. C., A. S. Orange, G. M. Hoversten, and H. F. Morrison, 1998, Marine magnetotellurics for petroleum exploration, Part I: A sea-floor equipment system: Geophysics, **63**, 816–825.

Constable, S. C., R. L. Parker, and C. G. Constable, 1987, Occam's inversion: A practical algorithm for generating smooth models from electromagnetic sounding data, Geophysics, **52**, 289–300.

Constable, S. C., and C. J. Weiss, 2006, Mapping thin resistors and hydrocarbons with marine EM methods: Insights from 1D modeling: Geophysics, **71**, G43–G51.

Cox, C. S., S. C. Constable, A. D. Chave, and S. C. Webb, 1986, Controlled-source electromagnetic sounding of the oceanic lithosphere: Nature, **320**, 52–54.

Dickson, R. R., J. Meincke, S. A. Malmberg, and A. J. Lee, 1988, The 'Great Salinity Anomaly' in the northern North Atlantic 1968–1982: Progress in Oceanography, **20**, 103–151.

Duff, I. S., R. G. Grimes, and J. G. Lewis, 1989, Sparse matrix test problems: ACM Transactions on Mathematical Software, **15**, 1–14.

Edwards, N., 2005, Marine controlled source electromagnetics: Principles, methodologies, future commercial applications: Surveys in Geophysics, **26**, 675–700.

Eidsmo, T., S., Ellingsgrud, L. M. MacGregor, S. Constable, M. C. Sinha, S. Johanson, F. N. Kong, and H. Westerdahl, 2002, Sea bed logging (SBL), a new method for remote and direct identification of hydrocarbon filled layers in deepwater areas: First Break, **20**, 144–152.

Ellingsrud, S., T. Eidsmo, S. Johansen, M. C. Sinha, L. M. MacGregor, and S.

Constable, 2002, Remote sensing of hydrocarbon layers by seabed logging (SBL): Results from a cruise offshore Angola: The Leading Edge, **21**, 972–982.

Everett, M. E., and R. N. Edwards, 1993, Transient marine electromagnetics: the 2.5-D forward problem: Geophysical Journal International, **113**, 545–561.

Flosadottir, A. H., and S. Constable, 1996, Marine controlled source electromagnetic sounding 1. Modeling and experimental design: Journal of Geophysical Research, **101**, 5507–5517.

Freund, R. W., and N. M. Nachtigal, 1991, QMR: A quasi-minimial residual method for non-Hermitian linear systems: Numerische Mathematik, **60**, 315–339.

——, 1994, An implementation of the QMR method based on coupled two–term recurrences: SIAM Journal on Scientific Computing, **15**, 313–337.

Haber, E., and U. M. Ascher, 2001, Fast finite volume simulation of 3D electromagnetic problems with highly discontinuous coefficients: SIAM Journal on Scientific Computing, **22**, 1943–1961.

Hoversten, G. M., S. C. Constable, and H. F. Morrison, 2000, Marine magnetotellurics for base–of–salt mapping: Gulf of Mexico field test at the Gemini structure: Geophysics, **65**, 1476–1488.

Johansen, S. E., H. E. F. Amundsen, T. Røsten, S. Ellingsrud, T. Eidesmo, and A. H. Bhuyian, 2005, Sub-surface hydrocarbons detected by electromagnetic sounding: First Break, **23**, 31–36.

Key, K., S. C. Constable, and C. J. Weiss, 2006, Magentotelluric analysis of the Gemini prospect, Gulf of Mexico: Geophysics, **70**, B17–B27.

Langtangen, H. P., and A. Tveito, 1988, A numerical comparison of conjugate gradient-like methods: Communications in Applied Numerical Methods, **4**, 793–798.

MacGregor, L., and M. Sinha, 2000, Use of marine controlled-source electromagnetic sounding for sub-basalt exploration: Geophysical Prospecting, **48**, 1091–1106.

Mackie, R. L., J. T. Smith, and T. R. Madden, 1994, Three-dimensional electromagnetic modeling using finite difference equations: The magnetotelluric example: Radio Science, **29**, 923–935.

Madsen, N. K., and R. W. Ziolkowski, 1988, Numerical solution of Maxwell's equations in the time domain using irregular nonorthogonal grids: Wave Motion, **10**, 583–596.

——, 1990, A three–dimensional modified finite volume technique for Maxwell's equations: Electromagnetics, **10**, 147–161.

Mattiussi, C., 1997, An analysis of finite volume, finite element, and finite difference methods using some concepts from algebraic topology: Journal of Computational Physics, **133**, 289–309.

McGillivray, P. R., D. W. Oldenburg, R. G. Ellis, and T. M. Habashy, 1994, Calculation of sensitivities for the frequency-domain electromagnetic problem: Geophysical Journal International, **116**, 1–4.

Newman, G. A., and D. L. Alumbaugh, 1995, Frequency-domain modelling of airborne electromagnetic responces using staggered finite differences: Geophysical Prospecting, **43**, 1021–1042.

Sinha, M. C., P. D. Patel, M. J. Unsworth, T. R. E. Owen, and M. G. R. MacCormack, 1990, An active source electromagnetic sounding system for marine use: Marine Geophysical Research, **12**, 59–68.

Smith, J. T., 1996, Conservative modeling of 3-D electromagnetic fields, Part I: Properties and error analysis: Geophysics, **61**, 1308–1318.

Srnka, L. J., J. J. Carrazone, E. A. Eriksen, and M. S. Ephron, 2006, Remote reservoir resistivity mapping — An overview: The Leading Edge, **25**, 972–975.

Um, E. S., 2005, On the physics of galvanic source electromagnetic geophysical methods for terrestrial and marine exploration: M.S. thesis, University of Wisconsin.

Unsworth, M., and D. Oldenburg, 1995, Subspace inversion of electromagnetic data: Application to midocean-ridge exploration: Geophysical Journal International, **123**, 161–168.

Wang, T., and S. Fang, 2001, 3-D electromagnetic aniosotropy modeling using finite differences: Geophysics, **66**, 1386–1398.

Wang, T., and G. W. Hohmann, 1993, A finite-difference, time-domain solution for three-dimensional electromagnetic modeling: Geophysics, **58**, 797–809.

Ward, S. H., and G. W. Hohmann, 1988, Electromagnetic theory for geophysical applications, in M. Nabighian, ed., Electromagnetic methods in applied geophysics: SEG, 331–311.

Webb, S. C., S. C. Constable, C. S. Cox, and T. K. Deaton, 1985, A seafloor electric field instrument: Journal of Geomagnetism and Geoelectricity, **37**, 1115–1129.

Weiss, C. J., 2001, A matrix-free approach to solving the fully 3D electromagnetic induction problem: 71st Annual International Meeting, SEG, Expanded Abstracts, 1451–1454.

Weiss, C. J., and G. N. Newman, 2002, Electromagnetic induction in a fully 3-D anisotropic Earth: Geophysics, **67**, 1004–1114.

Woźniakowski, H., 1980, Roundoff-error analysis of a new class of conjugate-gradient algorithms: Linear Algebra and its Applications, **29**, 507–529.

Yee, K. S., 1966, Numerical solution of initial boundary value problems involving Maxwell's equations in isotropic media: IEEE Transactions on Antennas and Propagation, **AP-14**, 302–307.

Yee, K. S., and J. S. Chen, 1997, The finite-difference time-domain (FDTD) and the finite-volume time-domain (FVTD) methods in solving Maxwell's equations: IEEE Transactions on Antennas and Propagation, **45**, 354–363.

Yu, L., and R. N. Edwards, 1992, The detection of lateral anisotropy of the ocean floor by electromagnetic methods: Geophysical Journal International, **108**, 433–441.